

**Design, Progressive Modeling,
Manufacture, and Testing of
Composite Shield for
Turbine Engine Blade Containment**

**Summary of Research Report for
NASA Grant NCC3-744**

by

Dr. Wieslaw K. Binienda
The University of Akron
Civil Engineering Department
Akron, OH 44325-3905
Tel.: (330) 972-6693
wbinienda@uakron.edu

Dr. Erol Sancaktar
The University of Akron
Polymer Engineering Dept.
Akron, OH 44325-0301
Tel.: (330) 972-5508
erol@uakron.edu

ABSTRACT

An effective design methodology was established for composite jet engine containment structures. The methodology included the development of the full and reduced size prototypes, and FEA models of the containment structure, experimental and numerical examination of the modes of failure due to turbine blade out event, identification of materials and design candidates for future industrial applications, and design and building of prototypes for testing and evaluation purposes.

1. INTRODUCTION

A jet engine containment ring has to withstand very high-energy impact resulting from fragmented engine parts such as blade or rotary disc, and yet it is desirable to reduce its weight. The primary objective of this project was to design a containment ring to be filament wound using polymer-matrix composite materials. Initially, data from different commercially available engines were used to establish dimensions of a design prototype on which all calculations were based. Various design parameters were also defined as the input and/or output parameters in the analytical design process. Energy calculations were then carried out to establish the energy values incident from the impacting blades. The maximum load and moment values thus obtained were evaluated in terms of factors of safety (strength/stress ratio, R_{Lim}) in the basic pressure vessel-loading mode in conjunction with a composites design software called MIC-MAC prepared by Think Composites Publishers. Energy balance models were also used to account for the composite impact damage modes such as plugging and petaling. For optimization of lay-up configurations, various configurations for up to 4 different winding angles were considered with the number of plies varying from 1 to 6 for each angle. For material optimization, analysis was done for different fiber-resin combinations such as glass-epoxy, graphite-epoxy, etc. This process yielded optimum lay-up, winding angle, thickness, and fiber-resin types for the containment ring structure, based on the strength/stress ratio of the laminate for each case.

The final step in this study was to carry out impact testing of models, scaled down based on the same energy per unit volume value, in order to verify the outputs of the design process. Scaled-down prototypes were manufactured with the filament winding process using glass fiber and epoxy resin materials, and tested under dart-impact conditions. The experimental impact configuration was mainly in pressure mode, and the results followed the same trends predicted by the analysis.

2. ANALYTICAL PROCEDURE

2.1 Pressure based loading

A blade separated from the engine hub (rotor disk) would travel linearly before coming in touch with the containment shield. At this point, the leading edge of the blade, which is thin, might deform on contact. The blade would then rotate around the point of first impact until its trailing edge hits the shield. The trailing edge, which is thick and bulky, would cause most of the damage that occurs on the shield. This type of loading will be first interpreted as internal pressure on the shield. Another possible scenario could be the blade sweeping across the inner walls of the shield before coming to a complete stop. In this case also, the load can be interpreted in terms of internal pressure on the shield. Internal pressure can be obtained by dividing the kinetic energy by the affected volume of the containment ring. It is difficult to accurately estimate the volume of the ring that would be directly affected by impact and absorb energy. For a first approximation, it will be represented as a $\frac{\theta}{360} \left(\frac{L_{affected}}{L_r} \right)$ fraction of the total shield volume,

$$\text{i.e., Affected Volume} = \frac{\theta}{360} \left(\frac{L_{\text{affected}}}{L_s} \right) \pi T_s D_s L_s$$

In the equations above, θ is the angle swept by the blade as it moves along the inner walls of the shield. This value will also be called "degree of coverage" in the calculations to be presented henceforth. Calculations were made for affected volume using 90 and 180 degrees as values for the degree of coverage. Since it is difficult to accurately estimate the axial length affected, calculations were carried out for different axial length values ranging from the blade width (affected length, $L_{\text{affected}} = W_b$) to the shield length ($L_{\text{affected}} = L_s$). The third parameter required in the calculation of the affected volume is the thickness of the shield, T_s , which in fact is an output of this optimization process. Hence, iterations were carried out for thickness values from 1 to 40 mm shield thickness. The pressure values obtained by the above procedure were then used as inputs to the MIC-MAC Pressure Vessel module.

2.2 Pressure- Torque based loading

Another possible impact scenario could be the one in which the blade does not deform on first impact and hence the thick rear section of the blade does not create a normal force on the containment shield. In such a case, the blade would exert both torque as well as pressure on the shield. The velocity of the blade, v_b , can be resolved into two components, normal to the containment shield (v_{bn}) and tangential to the containment shield (v_{bt}). These velocity components contribute to kinetic energies in the normal and tangential directions respectively. If θ is the angle traversed by the blade before first impact, then the turbine configuration requires that,
 $v_{bt} = v_b \cos \theta$, and $v_{bn} = v_b \sin \theta$.

Kinetic energy in the tangential direction contributes to the torque acting on the containment shield, whereas that in the normal direction contributes to the pressure.

The shear stress τ can be calculated using $\tau = \frac{E_{kt}}{V_{\text{affected}}}$.

Thus, the torque value can be calculated as $\left\{ \frac{\pi}{2} \tau D_s^2 T_s \right\}$.

The normal pressure value is given by $\left\{ \frac{E_{kn}}{V_{\text{affected}}} \right\}$.

Using the formulae discussed above, calculations were done for pressure and torque with affected volume fractions ($V_{\text{affected}} / V_s$) ranging from 0.1 to 0.5, and thickness values ranging from 2 mm to 22 mm. These values were then used as input to MIC-MAC Pressure Vessel module. The shield length is taken as half of the actual length $\frac{1}{2}L_s$ because of the way the torque acts on the cylinder.

2.3 Simple Plugging-petalling Model

Consider the penetration of a thin plate, where the target is dished away from the oncoming projectile. An approximation of the work done to bend the plate can be

calculated by considering the bending of the plate through 90° at diameter d in dishing (petalling)¹,

$$W_{\text{petal}} = \frac{\pi}{8} d h \sigma_0 (d + \pi h)$$

where, d = diameter of the impinging cylinder, h = thickness of the shield and σ_0 = tensile strength of the shield. Plug separation can occur by a number of different fracture mechanisms. An estimate of the work done in adiabatic shear (plugging), W_{plug} , is given by

$$W_{\text{plug}} = \frac{\pi}{2\sqrt{3}} d h^2 \sigma_0.$$

Energy of the blade before impact when divided by the work done during plugging and petalling, gives the strength/ stress ratios, R, for each case,

$$R_{\text{petal}} = \frac{E_k}{W_{\text{petal}}}, \text{ and } R_{\text{plug}} = \frac{E_k}{W_{\text{plug}}}.$$

For calculations based on this model, the value of the hole diameter d, was assumed to be equal to the width of the blade. Tensile strength of the composite material was calculated using MIC-MAC In-plane module. By using lay-up configuration and part thickness as inputs, the values of strength at design limit in 1-1 direction obtained from MIC-MAC were taken as tensile strength values for the material.

2.4 Hagg & Sankey Model for Ballistic Perforation

Hagg and Sankey^{2,3} developed an analytical model to simulate the containment of disk fragments in turbines. This model states that the containment of projectiles by cylindrical shells is a two-stage process. The first stage involves inelastic impact. The shell will be perforated if the kinetic energy loss in momentum transfer is greater than the strain energy for local shear and compression of the shell³. If perforation does not occur in stage 1, then the process enters stage 2 during which the energy is dissipated in plastic tension strain over extended volumes of the shell material.

2.4.1 Criterion for non-perforation in stage 1:

The criterion for non-perforation in stage 1 is given by,

$$E_s + E_c > \Delta E_1$$

where, E_s is the shear energy of a ductile material and E_c is the energy required to strain the material in compression.

2.4.2 Containment criterion in stage 2:

In stage 2, failure is due to tensile strain.

Strength/ stress ratios can be determined in terms of energy required for failure in each stage divided by energy loss of the blade in each stage.

$$R_1 = \frac{E_s + E_c}{\Delta E_1}, \text{ and } R_2 = \frac{E_t}{\Delta E_2}$$

3. ANALYTICAL RESULTS

Similar optimum lay-up configurations were obtained for pressure, simple petal-plug and Hagg and Sankey approaches, when a 20 mm thick, $[0/90/45/-45]$ glass-epoxy laminate was considered. With these approaches, the $[0_1/90_6/45_1/-45_1]$ configuration was found to have the highest strength/ stress ratio and the optimum lay-up remained the same irrespective of thickness. However, in the case of the pressure-torque loading approach, different optimum lay-up configurations were obtained for different laminate thickness. For example, $[0_1/90_6/45_1/-45_1]$ lay-up was found to be the best for 4 mm glass-epoxy laminate, while $[0_1/90_2/45_6/-45_2]$ was the best configuration for a 22 mm thick glass-epoxy laminate.

In case of pressure loading condition, the addition of 0° plies resulted in a decrease in the R/Lim values. For a 20 mm thick, $[0_X/90_6/45_1/-45_1]$ glass-epoxy laminate, the R/Lim value decreased by approximately 37% as the number of 0° layers, X, increased from 1 to 6. With the addition of 45° layers, R/Lim also showed a decrease of approximately 30%. However, the addition of 90° plies to the laminate resulted in an increase in the R/Lim values. In the case of a 20 mm thick, $[0_1/90_X/45_1/-45_1]$ glass-epoxy laminate, R/Lim increased by 64% as X changed from 1 to 6. Thus, the laminate strength was found to be more sensitive to changes in 90° layers as compared to changes in 0° and 45° layers.

Pressure, simple petal-plug and Hagg and Sankey approaches, all predicted the laminate strength to increase with an increase in the winding angle (Tables 1, 2). As the value of X increased in a $[0/90/X/-X]$ laminate, the R/Lim values also increased. Based on the pressure loading approach, the composite $[0_1/90_6/45_1/-45_1]$ ranked 87th in a list of 6480 lay-up configurations considered, which had the X layer angles changing from 45° to 65° . In contrast, the $[0_1/90_6/65_1/-65_1]$ laminate ranked 1st in the same list. The R/Lim value increased by 254% for a 20 mm thick $[0_1/90_6/X_1/-X_1]$ lay-up under in-plane tensile load, when the winding angle, X, was changed from 30° to 80° . The simple petal-plug model also predicted an increase in the R/Lim values by 22% against petalling failure, and 17% against plugging failure for the same laminate. The Hagg and Sankey model indicated an approximate 22% rise in R1 and R2 values.

The pressure-torque loading condition accounted for maximum torque on the shield and was thus, most relevant in determining the optimum winding angle. For all the laminates considered, the R/Lim values increased up to a certain value, and then decreased again, as the angle was changed from 30° to 80° . The 60° and 55° laminates showed the highest strength, while 65° and 45° laminates were ranked lower than 11th and 166th respectively, among the 6480 configurations considered. For example, 48° was found to be the best winding angle for a 22 mm thick, $[0_1/90_6/X_1/-X_1]$ glass-epoxy laminate. On the other hand, $[0_1/90_1/X_4/-X_1]$ configuration was found to be the best laminate for 22 mm thickness, with optimum winding angle being approximately $\pm 60^\circ$.

For pressure based loading, the best glass-epoxy lay-ups had R/Lim values greater than 1.00 for thickness of 20 mm and above. For a $[0_1/90_6/45_1/-45_1]$ laminate, R/Lim increased by 79% and 83% when thickness increased from 15 mm to 25 mm in 5 mm increments, respectively.

The best glass-epoxy lay-ups had R/Lim values greater than 1.00 at 10 mm thickness based on the pressure-torque approach.

In optimizing the fiber-matrix material combinations, the carbon-epoxy laminates were found to possess the highest strength based on all the approaches except for pressure-torque loading, which yielded boron-epoxy as the best combination. Kevlar-epoxy was the weakest laminate in all approaches, followed by glass-epoxy (Table 3).

For a 20 mm thick $[0_1/90_6/45_1/-45_1]$ laminate under pressure loading condition, the R/Lim values for carbon-epoxy, graphite-epoxy (T3N52) and Kevlar-epoxy were found to be 4.5, 3.8 and 0.6 times that of glass-epoxy respectively. Similar ratios were observed for other loading conditions. All fiber-resin combinations showed increase in strength with an increase in laminate thickness.

4. SCALE-MODEL TESTING

The experimental results obtained from the testing of scale model specimens, showed the same trends as predicted analytically. It was observed that, all specimens showed complete penetration at 13.6 Nm, and no penetration at energies up to 9.7 Nm. The lay-ups $[0_1/90_2/50_1/-50_1]$ and $[0_1/65_2/-65_2]$ were penetrated only at 13.6 Nm. The laminate $[90_3/65_1/-65_1]$ exhibited R/Lim values greater than 1.75, and was the highest R/Lim value for the lay-up configurations considered. On comparing the lay-ups $[90_3/65_1/-65_1]$ and $[0_3/65_1/-65_1]$ it was observed that R/Lim values increased with an increase in the number of 90-degree layers, and with a decrease in number of 0-degree layers. Similarly, when comparing $[0_1/90_4]$ and $[0_1/65_2/-65_2]$ lay-up configurations, it was noted that R/Lim increased with an increase in the number of 65-degree layers (Tables 4, 5).

Details on the findings summarized so far can be found in reference⁴.

5. MANUFACTURING OF THE PROTOTYPE RING

5.1 The Mandrel

The mandrel was designed to be collapsible in four pieces as shown in Figure 1. This facilitated the separation of the cured ring from the rigid mandrel. The mandrel was manufactured using 6.35 mm thick steel in order to maintain the dimensions and shape of the containment ring.

5.2 Mandrel-Shaft

A 2.29 m long, 6.35 cm diameter steel shaft was machined with key slots for keyed assembly with the mandrel as shown in Figure 2. One end of the shaft was milled flat on three (120° apart) sides to avoid slippage in the filament winder chuck.

5.3 Mandrel-Handling System

Since the mandrel/ring assembly weighs over 300 kg, a mandrel-handling system had to be designed and constructed. For this purpose, a one-ton jib crane with one-ton motorized trolley, and a one-ton electric hoist was constructed and installed. The hoist/trolley system has one hanging 4-button pendulum control

with all functions together. A spreader bar with provision to attach to the mandrel shaft and the hoist was also designed and installed. This system allowed efficient transport of the manufactured ring to the nearby Despatch digitally-controlled, walk-in thermal-curing chamber. This integrated handling system is shown in Figure 3.

5.4 Mandrel-Cart

An existing oven-cart was modified to accommodate the mandrel shaft, and to keep the mandrel from moving out of the supports. Sintered bronze blocks were incorporated into the cart to support the mandrel assembly. This assembly is shown in Figure 4.

5.5 Modifications to the Curing System (Despatch Cure-Chamber)

A new digital thermal controller was installed on the Despatch cure-chamber to be able to cure the Hexcel IM6/3501-6ATL; 35%; 140 AW; 0.125" prepreg material used in winding. This material requires a complex cure schedule with dual ramps, and hold times.

In order to induce uniform cure with no shape change, a mandrel rotating system was designed, fabricated, and installed to turn the mandrel while in the oven. This system is made up the following components: a 110 volt gear-motor, a gear belt, 2 drive pulleys, one base-plate for the motor, and an OSHA compliant belt-guard. The base-plate and the belt guard was mounted to the floor with flush-mount anchors and thumb screws. This assembly is shown in Figure 4.

5.6 Mandrel Poles

In order to be able to use the non geodesic winding pattern available on the CADWIND NG Pro program at relatively high winding angles (60°), polypropylene end poles were engineered, and attached to the mandrel using eye-bolts (Figures 5 and 6). The poles were further shaped using heat resistant fibrous mattes attached by duct tape. The resulting assembly is shown in Figures 7 and 8, with the engineered poles reducing the mandrel diameter down to (approximately) 0.635 m from 0.914 m, over an axial distance of 0.28 m.

5.7 Ring Materials

Based on our design optimization we chose graphite/epoxy prepreg material for the containment ring. Since the Hexcel IM6/3501-6ATL;35%:140AW;0.124" prepreg is commonly used by aircraft engine manufacturers such as GE, we decided to use this

specific material for the manufacture of our prototype ring. This 3.175 mm wide prepreg was used in $\pm 60^\circ$, and 90° layers winding. The 0° layers were hand laid using the IM6-G/3501-6;35%;145AW;12"MT5 version.

5.8 CADWIND

Ellipsoidal pole option was used in "Create Mandrel" mode. The pole-opening diameter was 647 mm and the length of the ellipsoidal extension was 120.65 mm. In "Material Parameters" mode, the number of rovings was 8. The "non-geodesic" option was used in "Winding" mode for winding the 60° layers, which allowed, approximately 103% coverage. The 90° layers were wound using the "Circumferential" option. The file created in this fashion was saved as a *.dat file. This file operates the filament winding machine under CMC.EXE mode according to the file created in the Cad Wind software. The 90° layers were wound using the "Circumferential wind" option, and hand lay-up followed by manual roller compaction and smoothing was used for the 0° lay-up. The prepreg line-tension was set to 53.4 N. This allowed tight and compact winding.

The total ring lay-up is shown in table below.

Ply Angle	+60	-60	0	90	
Number of Layers	6	6	1	1	Inside Layer
	6	6	1	1	
	6	6			Outside Layer

5.9 Curing

Curing was done in Despatch cure chamber equipped with the rotating mechanism (Fig. 4). The cure schedule used was as follows:

Heat-up to 116°C at $(1.8\text{--}3^\circ\text{C})/\text{min}$

Hold 70 min

Heat-up to 177°C at $(1.8\text{--}3^\circ\text{C})/\text{min}$

Hold 120 min

Cool to ambient with doors closed.

5.10 Pole Removal

The cured assembly was placed back on the filament winder, and the poles were machined off using a 15.24 cm D, 2.3 mm thick diamond cutter rotating at 10,000 rpm. The high-grade diamond wheel was continuous, and without teeth, suitable for cutting glass. The cutter assembly slid along the 15.24 x 10.16 cm rail along the bottom of the filament winding machine, locking into position with a T-handle set screw, when needed. The cutter was mounted on a manual linear slide with 20.3 cm-travel, and engaged into the cut by a manual crank (Fig. 9). The cured ring assembly was rotated in direction opposite to the rotation of the cutter by the filament winder during machining. Cut dust

was collected by using several vacuum cleaners during machining. The average ring thickness was measured subsequently as approximately 8 mm.

6. THE PROTOTYPE

Pictures of the manufactured prototype are shown in Figures 10 and 11.

Table 1. R/Lim values for the proposed design alternatives with glass-epoxy materials ($T_s = 20$ mm, [0/90/X/-X] lay-up)

Lay-up	Optimum Winding Angle (degrees)	Pressure based loading R/Lim	Pressure-torque loading R/Lim	Simple petal-plug model		Hagg and Sankey model	
				Rplug	Rpetal	R1	R2
1611	48	1.60	4.33	0.23	1.05	0.99	0.48
1511	48	1.54	4.88	0.22	1.01	0.96	0.46
1621	52	1.56	5.22	0.22	0.10	0.97	0.47
2611	48	1.47	3.96	0.21	0.96	0.91	0.44
1411	48	1.47	5.61	0.21	0.96	0.91	0.44
1622	60	1.63	6.51	0.23	1.06	1.01	0.49
1512	62	1.63	5.77	0.23	1.06	1.01	0.49
1613	66	1.68	5.62	0.24	1.09	1.05	0.50
2621	50	1.43	4.99	0.20	0.93	0.88	0.42
2511	48	1.41	4.41	0.20	0.92	0.87	0.42
1623	68	1.72	6.34	0.24	1.12	1.07	0.51

Table 2. R/Lim values for the proposed design alternatives with graphite-epoxy (T3N52) materials ($T_s = 20$ mm, [0/90/X/-X] lay-up)

Lay-up	Optimum Winding Angle (degrees)	Pressure based loading R/Lim	Pressure-torque loading R/Lim	Simple petal-plug model		Hagg and Sankey model	
				Rplug	Rpetal	R1	R2
1611	48	6.08	16.45	0.87	3.99	3.76	1.82
1511	48	5.85	18.54	0.84	3.84	3.65	1.75
1621	52	5.93	19.84	0.84	0.38	3.69	1.79
2611	48	5.59	15.05	0.80	3.65	3.46	1.67
1411	48	5.59	21.32	0.80	3.65	3.46	1.67
1622	60	6.19	24.74	0.87	4.03	3.84	1.86
1512	62	6.19	21.93	0.87	4.03	3.84	1.86
1613	66	6.38	21.36	0.91	4.14	3.99	1.90
2621	50	5.43	18.96	0.76	3.53	3.34	1.60
2511	48	5.36	16.76	0.76	3.50	3.31	1.60
1623	68	6.54	24.09	0.91	4.26	4.07	1.94

Table 3. Thickness optimization for proposed design alternatives and for different materials (based on R/Lim = 1.25)

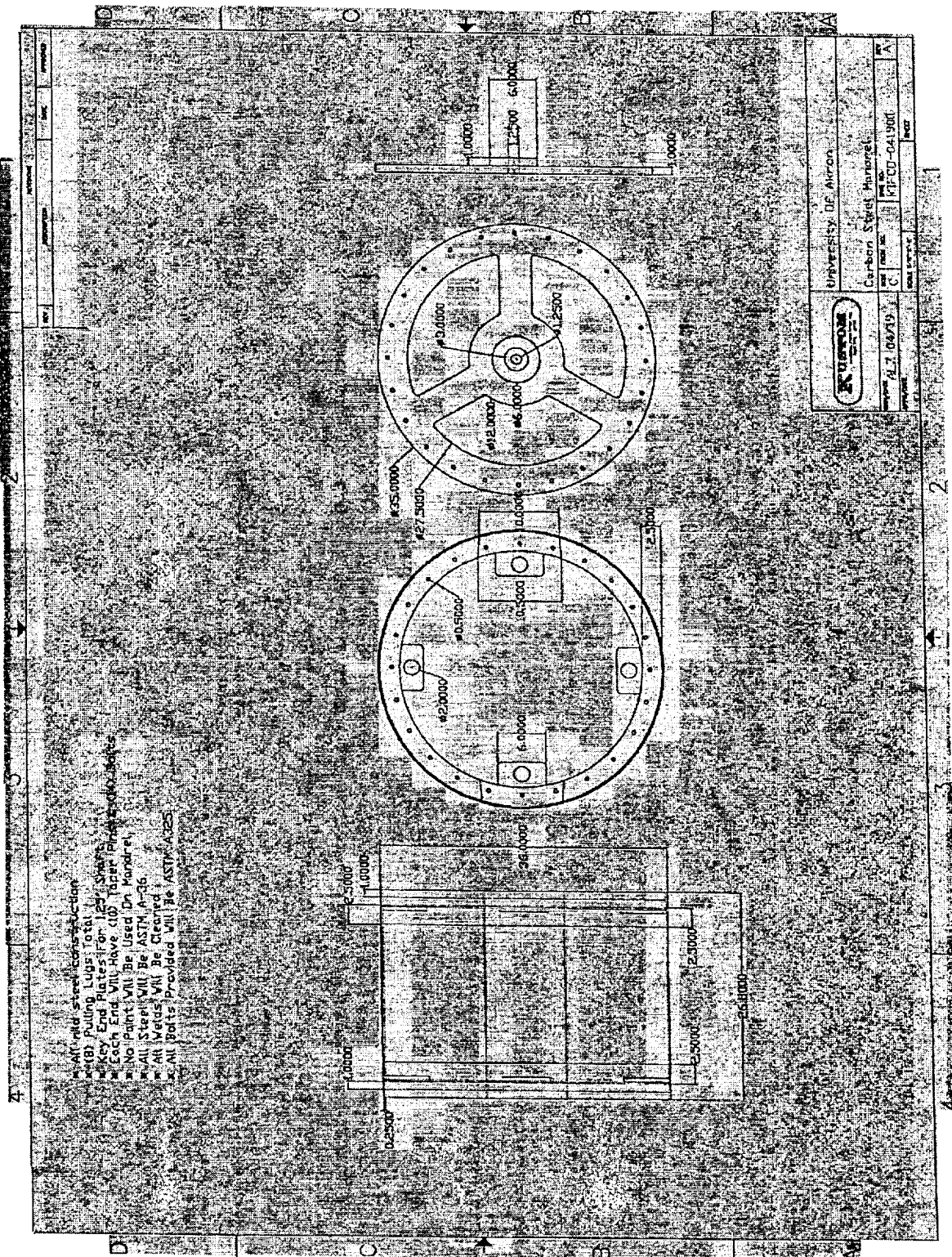
Lay-up	Opt. Wind. Angle(deg)	Pressure based loading T_s , mm				Pressure-torque loading T_s , mm				Simple petal-plug model T_s , mm				Hagg and Sankey model T_s , mm			
		IM6EP	T3N52	GLEP	KEVEP	IM6EP	T3N52	GLEP	KEVEP	IM6EP	T3N52	GLEP	KEVEP	IM6EP	T3N52	GLEP	KEVEP
1611	48	9	10	20	26	4	4	7	13	23	25	47	61	16	17	30	38
1511	48	9	10	20	26	4	4	7	14	24	25	47	61	16	17	31	38
1621	52	9	10	20	26	4	4	6	11	23	25	48	62	16	17	30	38
2611	48	10	11	21	27	4	4	7	16	26	27	49	63	17	18	33	39
1411	48	10	11	21	27	4	4	7	16	25	27	49	63	17	18	33	39
1622	60	9	10	19	25	4	4	7	11	24	25	45	62	16	17	30	38
1512	62	9	10	19	25	4	4	7	11	23	25	45	62	16	17	30	38
1613	66	9	10	19	25	4	4	7	12	23	24	46	60	15	16	29	37
2621	50	10	11	21	27	4	4	7	17	25	27	50	64	17	18	34	39
2511	48	10	11	21	27	4	4	7	17	25	27	50	64	17	18	35	39
1623	68	9	10	19	25	4	4	7	10	22	24	46	60	15	16	28	37

Table 4. Impact test results on model specimens based on 65° winding angle unless mentioned, and complete penetration occurring at the given energy level

Lay-up	Thickness (mm)	Impact Energy (Nm)				
		6.8	9.7	11.2	12.3	13.6
		Presence of complete penetration				
[0311]	1.36	No	No	No	Yes	Yes
[3011]	1.68	No	No	No	Yes	Yes
[1211]	1.55	No	No	Yes	Yes	Yes
[1211] _{50°}	1.79	No	No	No	No	Yes
[1400]	1.39	No	No	Yes	Yes	Yes
[1022]	1.70	No	No	No	No	Yes

Table 5. R/Lim values for model specimens

Lay-up	Thickness (mm)	Incident energy of the blade (scaled down based on volume) (Nm)	Highest energy at no penetration (from Table 5) (Nm)	R/Lim (column 4/ column 3)
[0311]	1.36	6.4	11.2	≥ 1.75
[3011]	1.68	7.9	11.2	≥ 1.42
[1211]	1.55	7.3	9.7	≥ 1.33
[1211] _{50°}	1.79	8.4	12.3	≥ 1.47
[1400]	1.39	6.5	9.7	≥ 1.49
[1022]	1.70	8.0	12.3	≥ 1.54



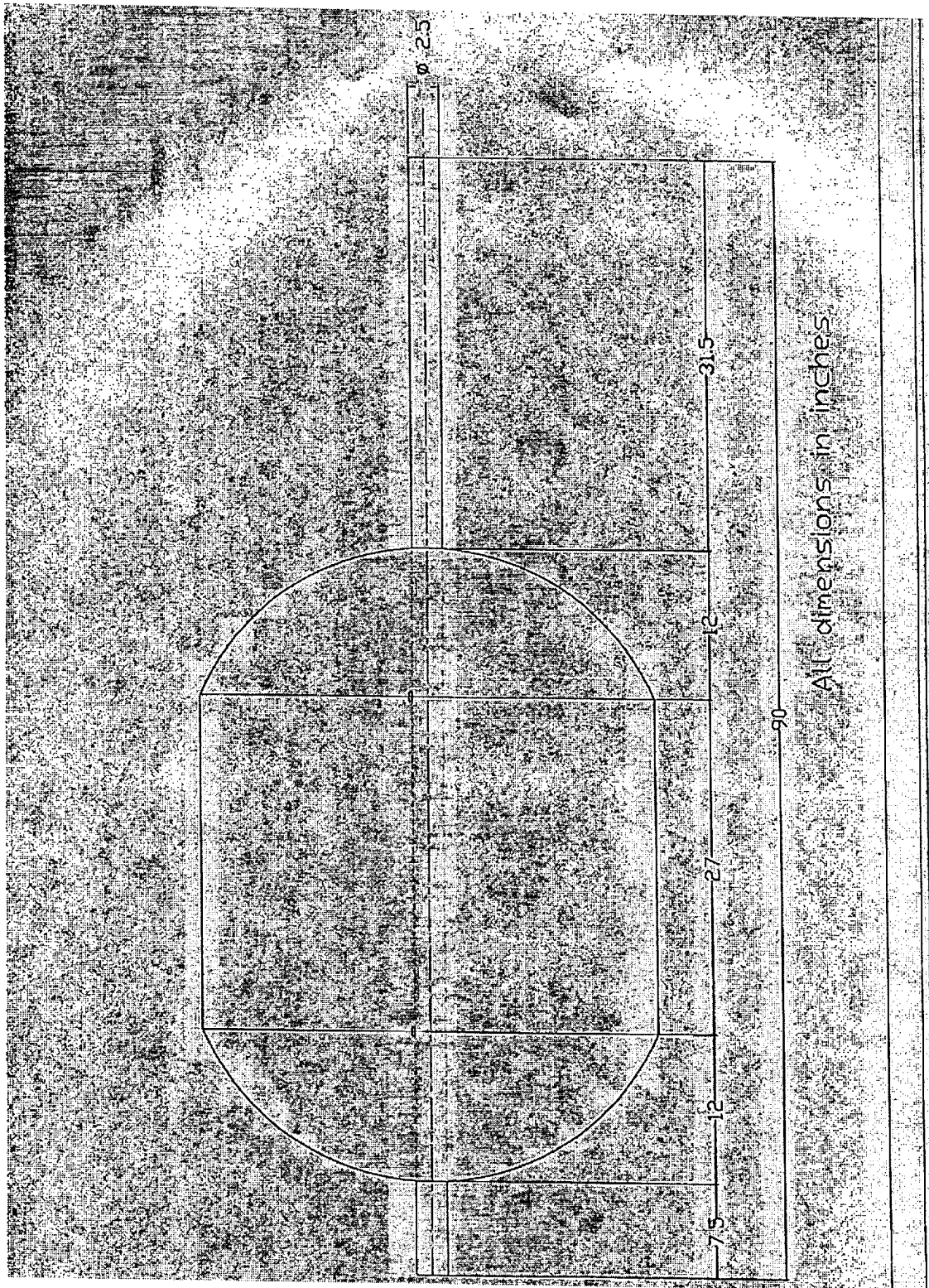
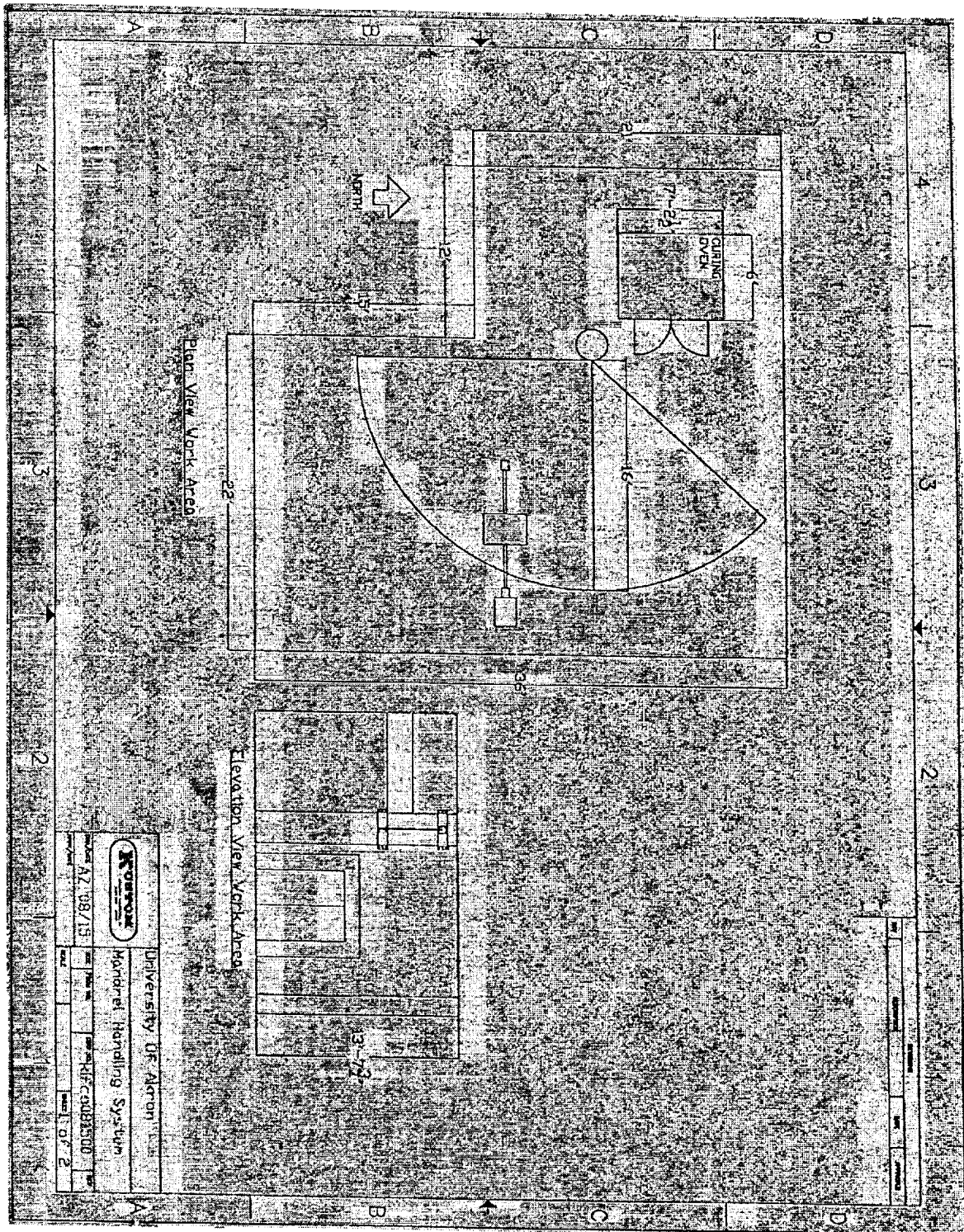


FIGURE 2. MANDREL/WOUND RING/SHAFT ASSEMBLY



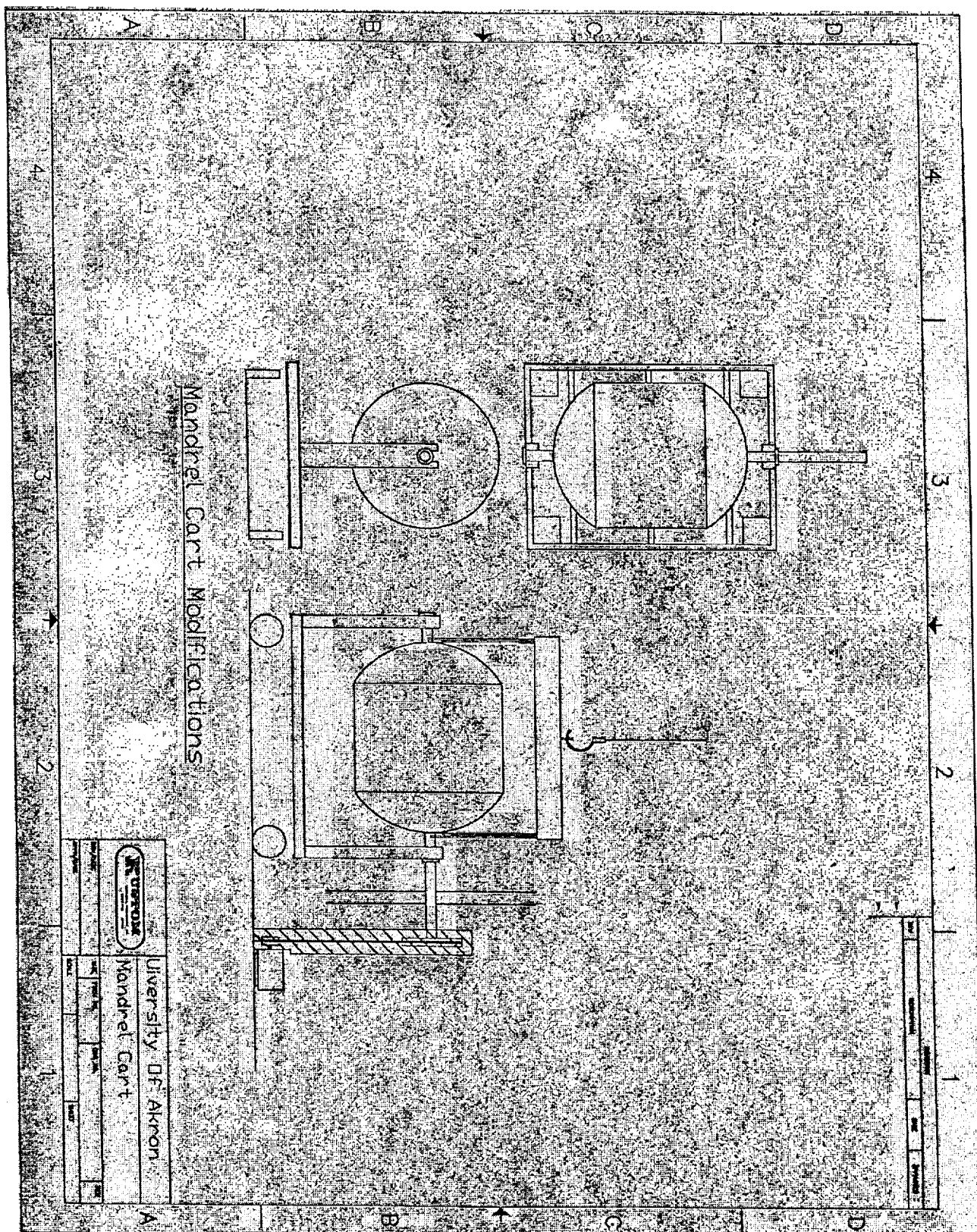


FIGURE 4. MANDREL CART AND THE ROTATING SYSTEM

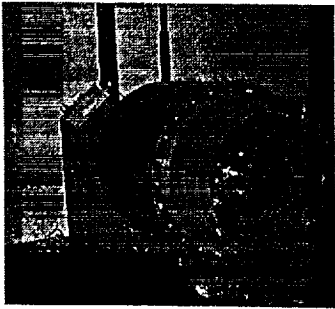


FIGURE 5. POLE, FRONT VIEW

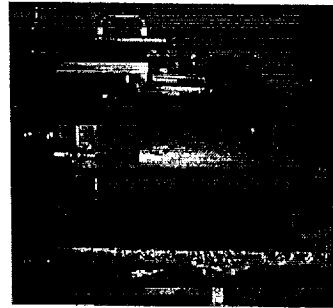


FIGURE 6. POLE, SIDE VIEW

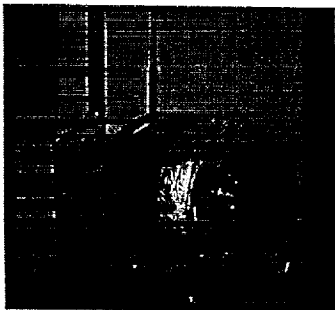


FIGURE 7. COMPLETE POLE,
FRONT VIEW

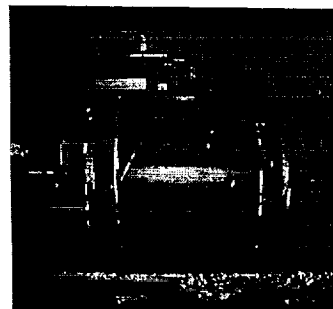


FIGURE 8. COMPLETE POLE,
SIDE VIEW

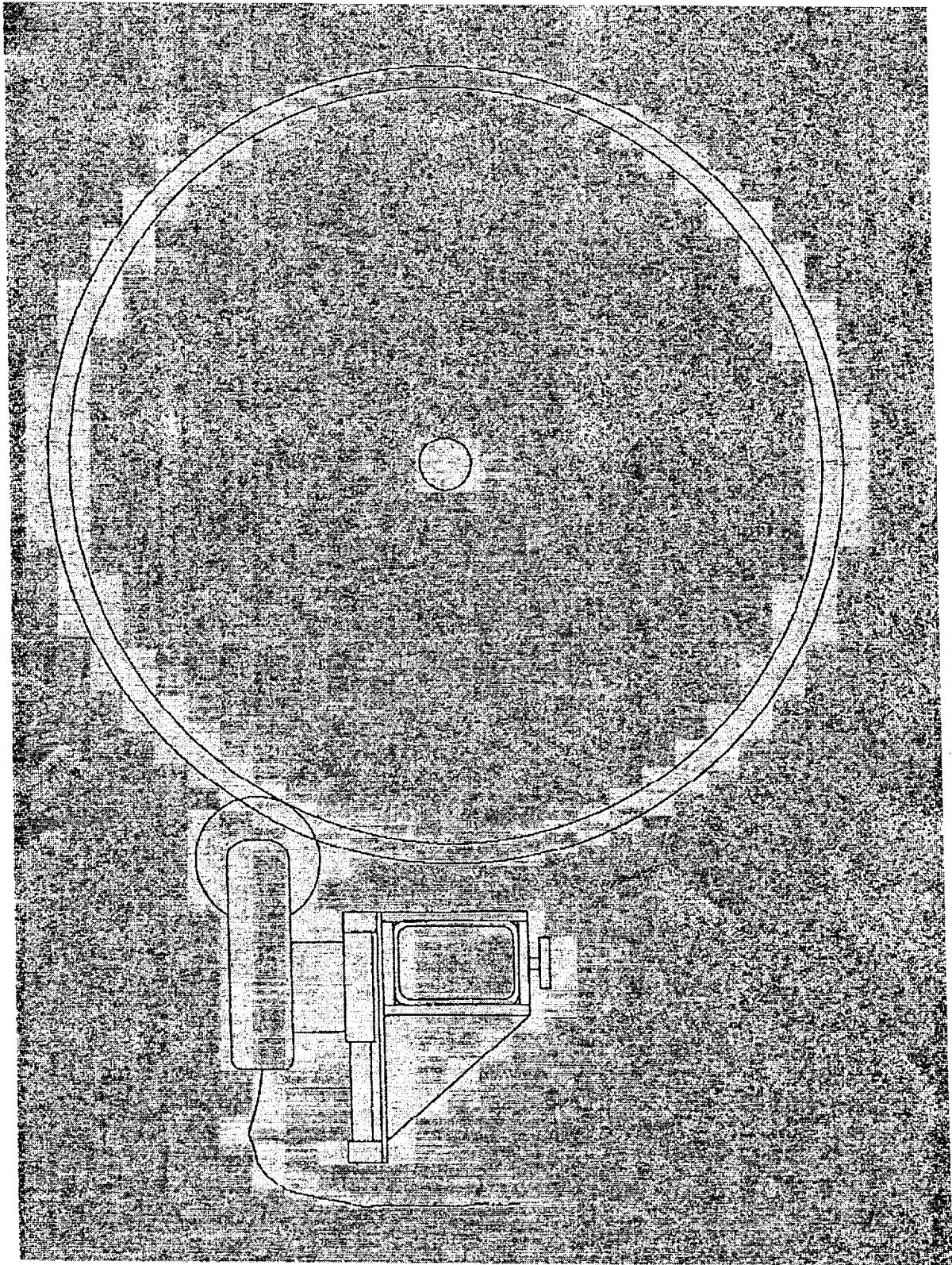


FIGURE 9. THE DIAMOND CUTTER ASSEMBLY

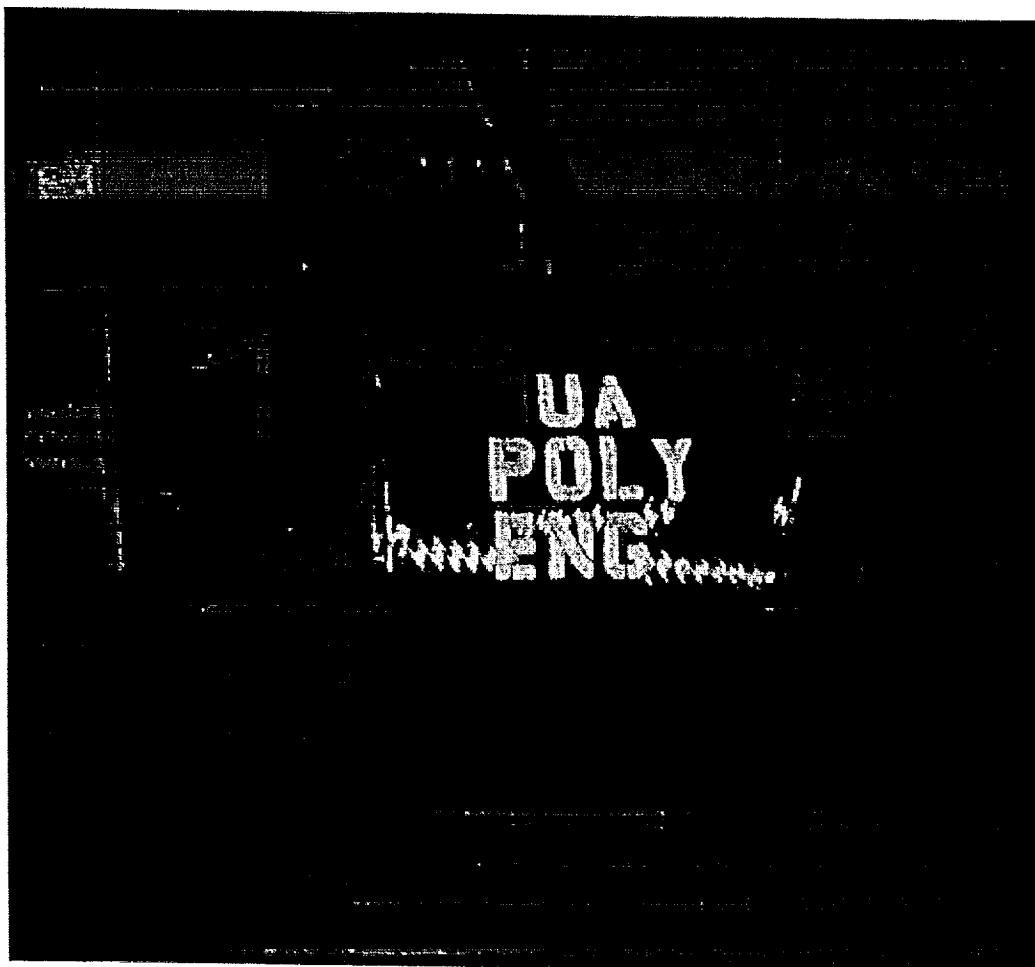


FIGURE 10. PROTOTYPE COMPOSITE-RING. SIDE VIEW

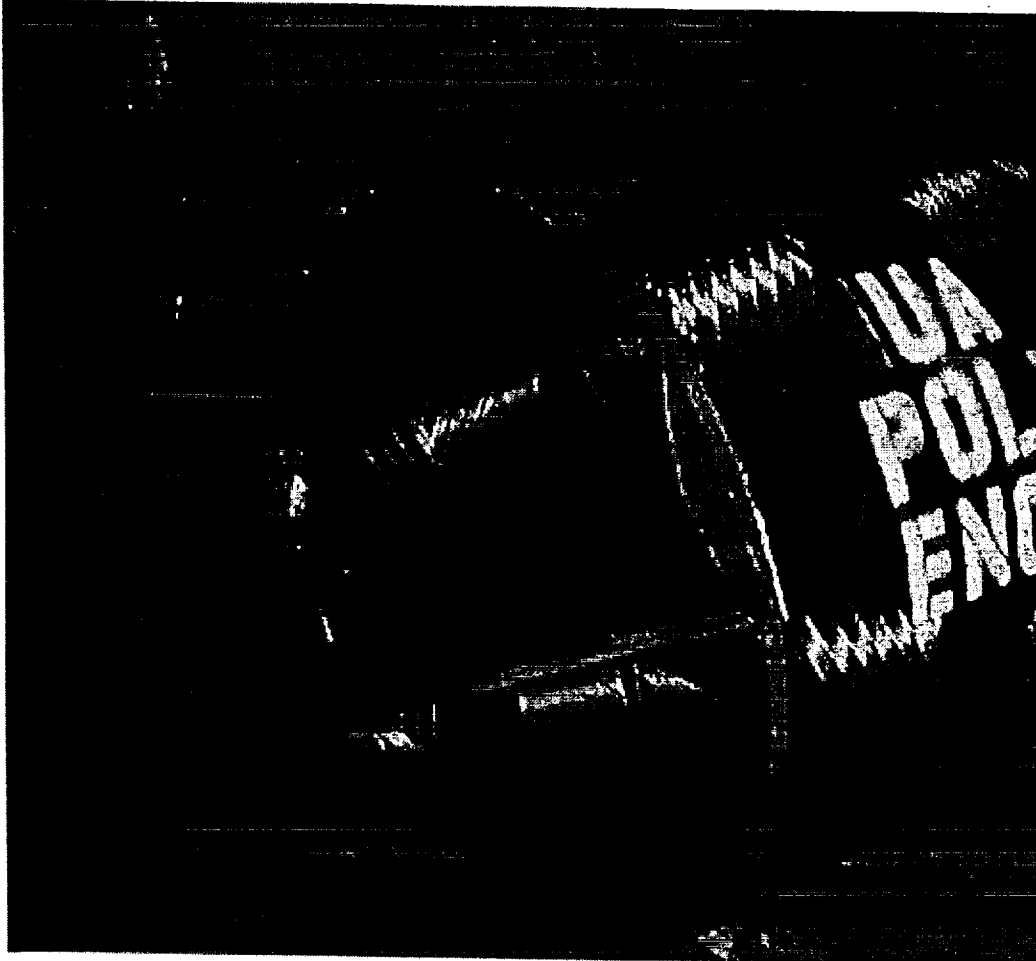


FIGURE 11. PROTOTYPE COMPOSITE-RING. PERSPECTIVE VIEW

7. EXPLICIT FEA MODEL

The dynamic response of a cylindrical composite shell impacted obliquely by a projectile has a vast practical background in aeronautical engineering. Recently, the impact on composite structures has been a subject of extensive research⁵⁻⁷. Lots of factors are involved in impact problems such as the projectile versus target structure mass ratio⁸, impact kinetic energy, the shape and length of the projectile, impact angle of obliquity, the dimension of target structure and its boundary conditions etc.

The interest of this research is focused on the influence of structure dimension and boundary condition on the overall dynamic response nature in the oblique impact of cylindrical composite shells. This has obvious practical and economic value in providing guidelines for choosing appropriate simple test models and planning experimental studies. No test data and report were shown to confirm whether a partial configuration of the structure could be used to represent the whole structure in a dynamic impact response test or analysis quantitatively so far. On the other hand, the complexity of impact problems also leads us to choose to combine theoretical, numerical and experimental approaches.

In this research, the numerical analysis of a composite laminate shell, subjected to the oblique impact by a thin flat rigid cylinder with a certain mass, is conducted using explicit dynamic method by ABAQUS. Five cases of analysis are performed for different dimensions of the shell configuration with both free and fully fixed boundary conditions. The strain and kinetic energy transfer and deforming history are examined from the numerical results. Especially, the influence of constraints on the cut boundary of partial configurations taken from the full shell is observed. Only the cases with free and fully fixed boundary condition are studied in consideration that the real constraints on the whole shell should lie between these two extreme situations. Both linear elastic and elastic-brittle failure material model are employed to obtain an understanding of the overall response of the shell and insight into the local damage and mutual influence between them. The localized damage/penetration is simulated using a brittle failure model combined with an element removal mechanism for failed part of the structure.

8. ANALYSIS MODEL

Illustrated in Figure 12 is a full-ring shell subcomponent proposed for testing of jet engine fan case by NASA Glenn Research Center, to evaluate the performance of a composite structure under blade-out loads. In this research, the transient impact response analysis of the subcomponent was performed using the commercial FEA code ABAQUS/Explicit. The impact

velocity was 182.88m/s (600ft/s) and the composite ring was taken to be 7.62×10^{-3} m (0.3") thick with the following properties, which are representative of a glass/epoxy laminate with a $0^\circ/90^\circ$ lay-up. $E_{11}=E_{22}=17237\text{Mpa}$ (2.5×10^6 lbf/in²), $G_{12}=6894.8\text{Mpa}$ (1.0×10^6 lbf/in²), $G_{13}=G_{23}=4136.88\text{Mpa}$ (6.0×10^5 lbf/in²), $\nu_{12}=\nu_{21}=0.14$ and $\rho=1715.58$ kg/m³ (0.00016 lbf s²/in⁴).

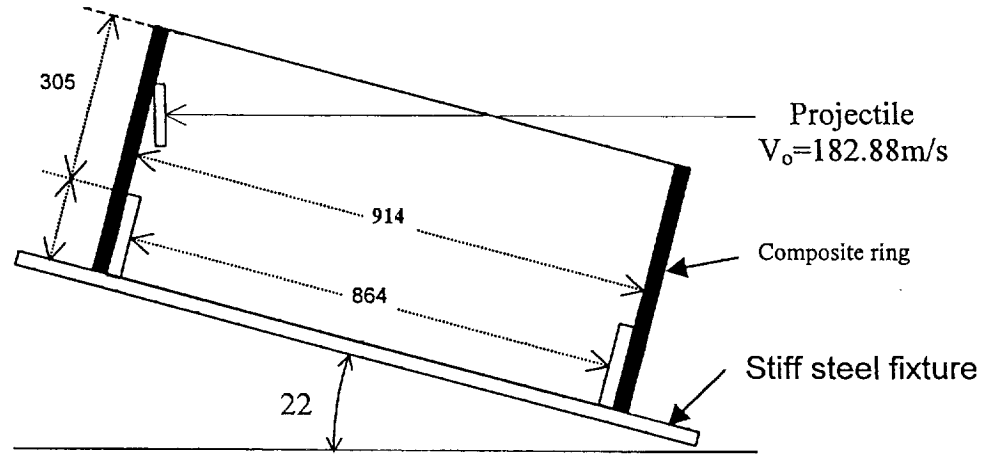


Figure 12: Illustration of the analysis model of the subcomponent (unit: mm)

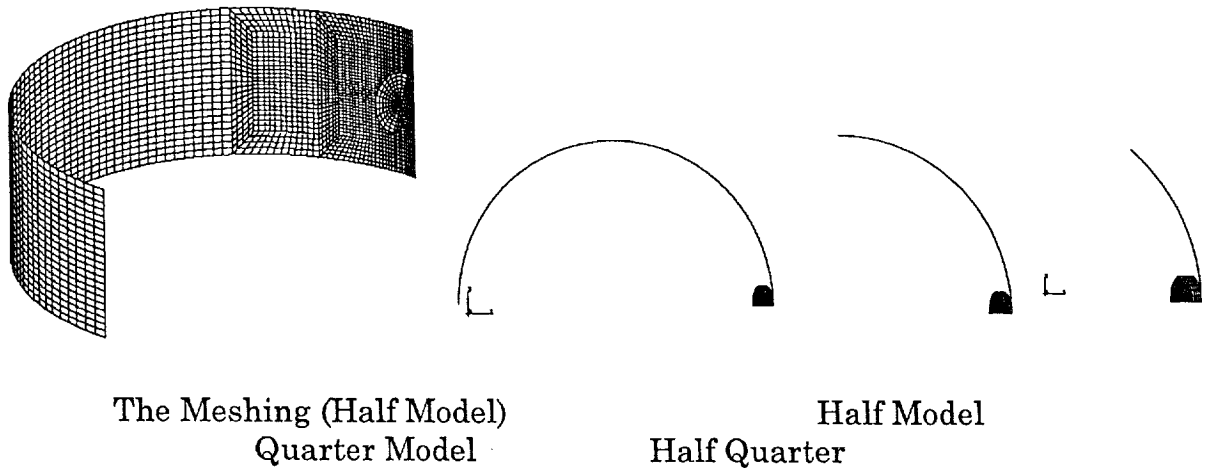


Figure 13: Symmetric FEA models of the structure

In addition to the pure elastic model, an elastic-brittle failure model was also included in the analysis to simulate the local damage. The brittle failure model was characterized by a tensile strength $\sigma_t^I = 275.8\text{Mpa}$ (40000

lbf/in²) and a failure strain $\epsilon_f = 0.023$. An element would be removed from the analysis process whenever all of its material points failed. The projectile was a flat circular cylinder with diameter of 114.3mm(4.5"), thickness of 19mm(0.75"), and mass of 0.854kg(1.9lb). It was ideally modeled as a rigid body with a density of 4366.7 kg/m³(0.0004086lbf s²/in⁴) since tracking waves and stress distributions in the projectile were not important in the present study. The shell was inclined at an angle of 22° to the horizontal.

In order to examine the effects of the shell dimension and boundary conditions, a half-shell and a quarter-shell model with both free and fixed end conditions at the cut boundary were analyzed in addition to the whole shell, as showed in Figure 13. All the analysis cases are listed in table 6. Because of the symmetry, only half of the structure geometry was modeled for all cases with symmetry condition about mid plane imposed. For simplicity, no friction between the projectile and shell during contact was considered. Four-node thin shell element S4R was used for the shell, and six-node and eight-node solid element C3D6 and C3D8R for the projectile. In addition, relax stiffness type of hourglass viscosity was used to restrict the element mechanisms, i.e. the zero-energy hourglass deformation mode, due to the degradation of first-order element integration. Also, in order to limit numerical oscillations due to discretization, a linear bulk viscosity with damping coefficient $b_1 = 0.0001$ was introduced.

TABLE 6
ANALYSIS CASES

Case	Structure	FEA model	Cut-end boundary	Bottom boundary
1	Whole	Half	-	Fixed
2	Half	quarter	Free	Fixed
3	Half	quarter	Fixed	Fixed
4	Quarter	Half quarter	Free	Fixed
5	Quarter	Half quarter	Fixed	Fixed

9. NUMERICAL RESULTS AND DISCUSSION

9.1 Deformation

In all figures, the small numbers 1-5 in the legends correspond to case 1-5, respectively. Units used in the figures are inch for displacement and lbf in for energy. Displacements for the projectile center and top edge of the shell

above the impact point are shown in Figures 14 and 15 for pure elastic analysis of case 1-5. For about the first 1.0ms the projectile is in contact with the shell. For times up to 1.5ms the response is very similar for the full shell and the half-shells with both free and fixed boundary conditions. The response of the quarter-shells is similar to that of the other configurations only for times below about 0.4ms, which corresponds to the initial impact of the upper edge of the projectile. These results suggest that a half-shell configuration could be used in place of a full shell to evaluate local damage, either free or fixed boundary conditions could be used. Figure 16 and 17 show the displacement history of the projectile center and the impact edge of the shells for all cases 1-5, respectively, when material failure was taken into account. It is seen that the responses for all the 5 cases are almost identical throughout the entire response, indicating that partial configurations could provide perfect approximation to the full model when local failure is involved.

It is noticed that for the partial shell configurations (case 2-5), those with free end boundary condition at the cut line provide a more similar response to the full shell (case 1) compared with the fixed end boundary condition. This indicates that the free-end condition provided a better approximation for a partial configuration to replace the full shell. This is valuable because free boundary is always convenient to be implemented in practice.

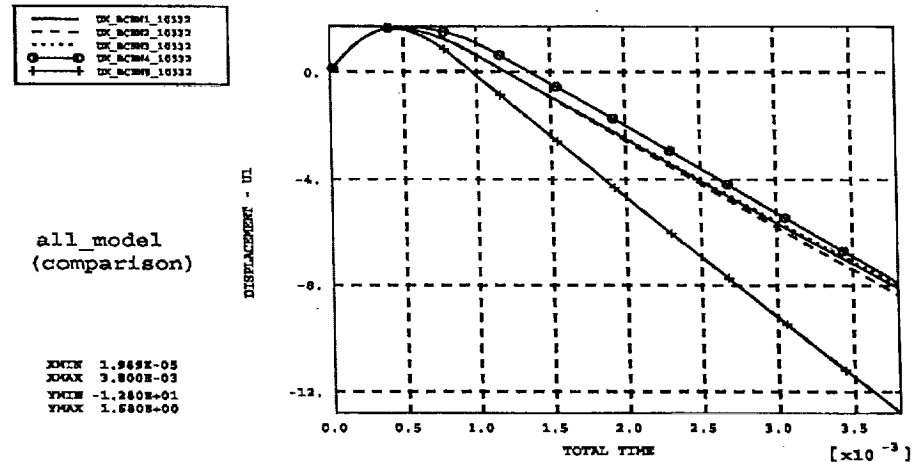


Figure 14: Comparison of displacement histories at the projectile center for case 1-5 (elastic)

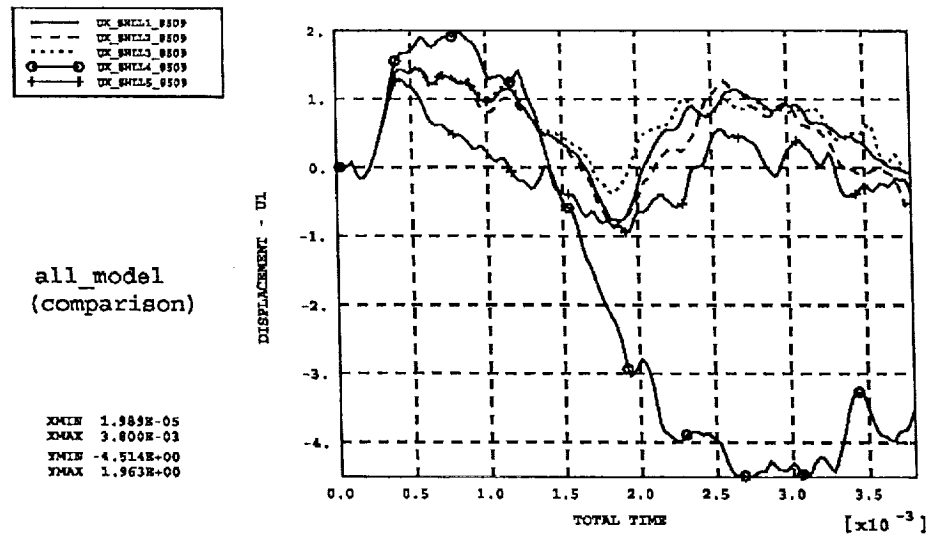


Figure 15: Comparison of displacement at the shell edge above the impact point for case 1-5 (elastic)

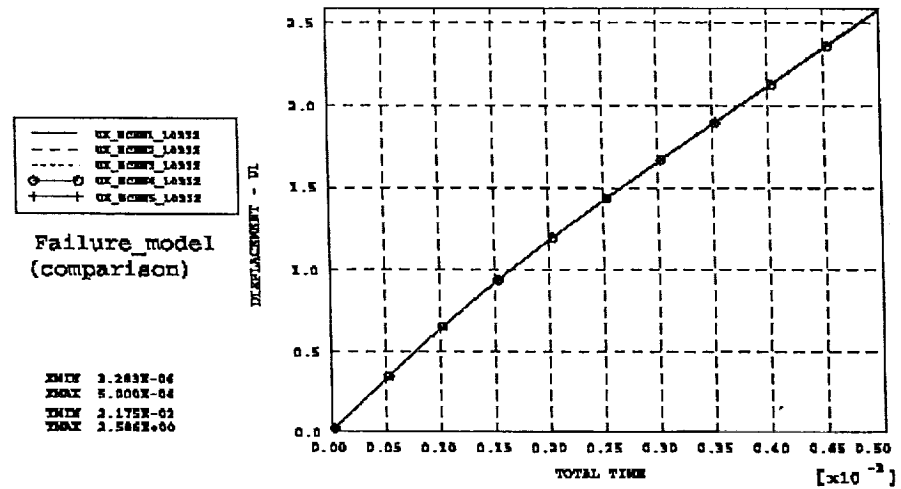


Figure 16: comparison of displacement at the projectile center for case 1-5 (brittle failure)

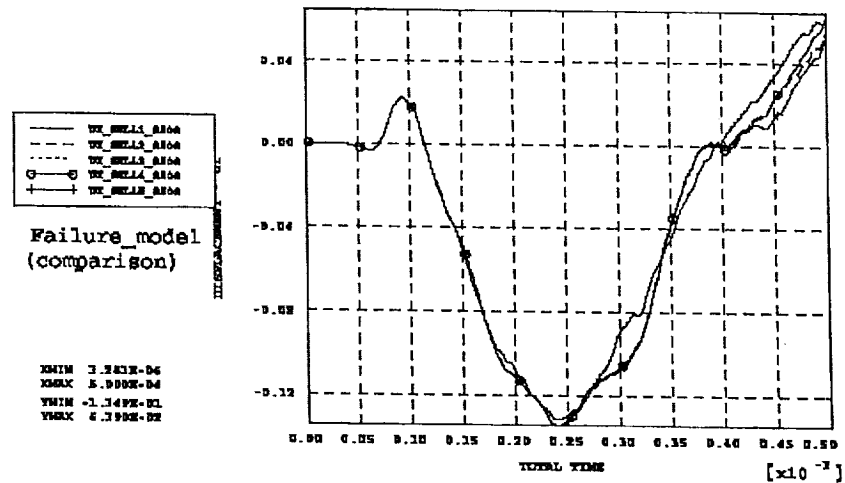


Figure 17: comparison of displacement at the impact shell edge for case 1-5 (brittle failure)

9.2 Energy transfer and absorption

An observation of strain and kinetic energy possessed by different portions of the shell helps understand the mechanism of energy transferring and distribution in the structure. Strain energies stored in arcs of various sizes around the impact area are shown in Figure 18 for the pure elastic full-shell configuration. The total energy (strain energy + kinetic energy) is shown in Figure 19. In Figure 18 the strain energy grows to a maximum value at about 0.45ms as the projectile comes into contact with the shell. The maximum strain energy is a little over half of the initial kinetic energy of the projectile. In Figure 19 the total energy in the full shell remains constant after about 1.0ms because the projectile has rebounded from the ring. It is seen that during impact and at the early stage of the later response, the 90°(half) arc portion of the shell almost possesses all the energy of the whole structure. As the deformation develops, the energy gradually transfers to the rest part of the structure.

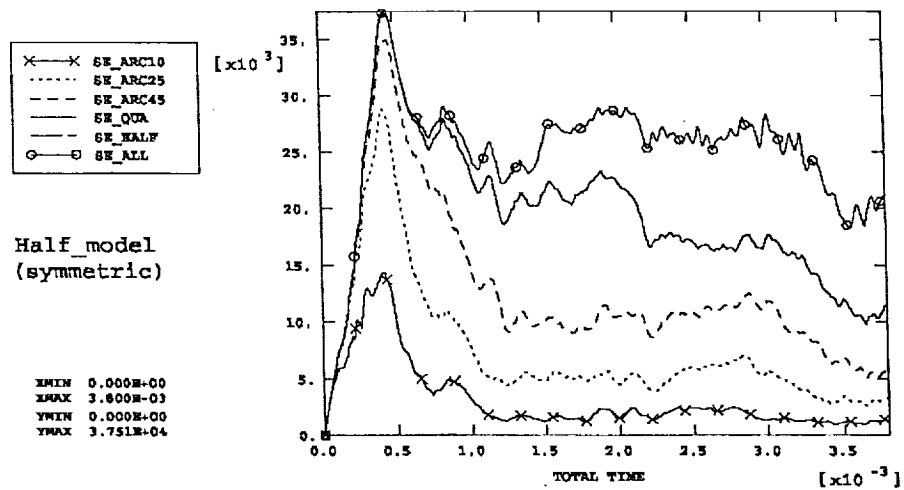


Figure 18: Strain energy in the arc of 10°, 25°, 45°, quarter, and half-shell (without and with the projectile included) for case 1(elastic)

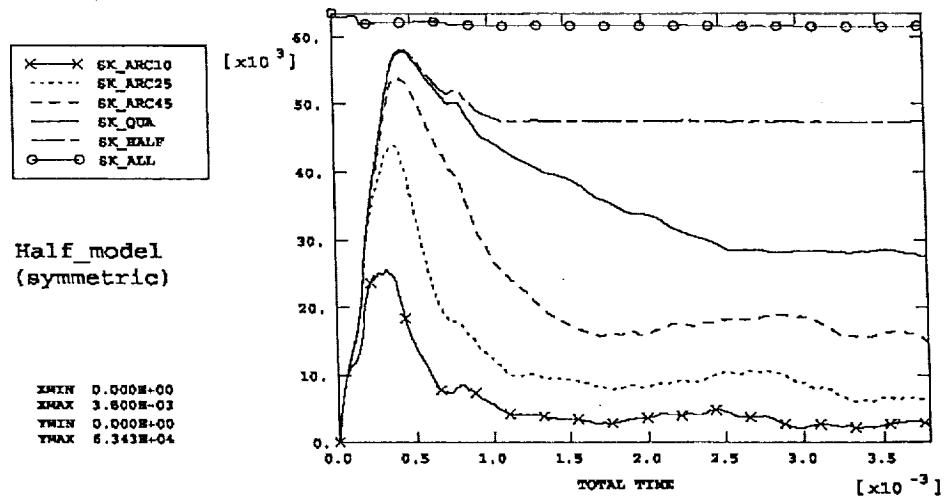


Figure 19: Strain and kinetic energy in the arc of 10°, 25°, 45°, quarter, and half shell (without and with the projectile included) for case 1(elastic)

10. CONCLUSIONS BASED ON THE FEA ANALYSIS

1. The initial local damage is not significantly affected by the boundary conditions while the subsequent deformation is strongly influenced by the boundary conditions.

2. A half shell could be used to replace the full shell when performing an impact experiment or analysis. Especially, an even better approximation could be obtained if local damage is involved.
3. Should a partial configuration be devised to simulate the response of the whole structure as a substitute, a free boundary condition could provide a closer result than a fixed boundary.
4. It is more reliable for a partial configuration to substitute the full shell when the localized damage is mainly concerned. This is because the impact times in the order of transition time for through-the-thickness waves is shorter than that required for the flexural wave reach the boundary⁵.

It must be stressed that the projectile versus shell mass ratio drastically changes the response style¹⁰. Also glass/epoxy composite material is strongly strain-rate dependent. How these factors affect the response characteristics is to be further reported.

11. REFERENCES

1. R. L. Woodward, in *High Velocity Impact Dynamics*, J. A. Zukas (ed), John Wiley & Sons, New York, 65, 1990.
2. A. C. Hagg and G. O. Sankey, *J. Eng. for Power*, (96), p. 114, 1974.
3. M. A. Amde, A. Mirmiran and T. Walter, *Nuclear Eng. and Design*, (178), p. 145, 1997.
4. N. Shah, "Design and Filament Winding of Composite Shield for Jet Engine Fan Blade Containment" M.S. Thesis, The University of Akron, Department of Polymer Engineering, 2001 (available through the UA Sci. & Tech. Library).
5. Abrate, S. (1994). *Appl. Mech. Rev.* 47(11), 517
6. Collombet, F., Lalbin, X. and Lataillade, J.L. (1998). *Composite Science and Technology*. 58, 463.
7. Christoforou, A.P and Yigit, A.SJ. (1998). *Solid and Vibration*. 217(3), 563
8. Nie, Z. and Yang, G. (1990). *Acta Mechanica Solida Sinica*. 3, 375
9. Beks, F-A. (1996). *FFA TN -29*, Bromma, Sweden
10. Olsson, R. (2000). *Composites part A*. 31, 879-887